Bayesian framework for inversion of second-order stress glut moments: application to the 2019 Ridgecrest sequence mainshock

James Atterholt[1] and Zachary E. Ross[1]

[1]Seismological Laboratory, California Institute of Technology, Pasadena, California, USA 91125

Key Points:

- We develop a Bayesian inverse scheme to solve for stress glut second moments of earthquakes using teleseismic data.
- We sample the positive-definite constrained posterior distribution using Hamiltonian Monte Carlo sampling and automatic differentiation.
- Using the 2019 Ridgecrest sequence mainshock as an example, we demonstrate the efficacy and utility of this inverse framework.

Corresponding author: James Atterholt, atterholt@caltech.edu

Abstract

We present a fully Bayesian inverse scheme to determine second moments of the stress glut using teleseismic earthquake seismograms. The second moments form a low-dimensional, physically-motivated representation of the rupture process that captures its spatial extent, source duration, and directivity effects. We determine an ensemble of second moment solutions by employing Hamiltonian Monte Carlo and automatic differentiation to efficiently approximate the posterior. This method explicitly constrains the parameter space to be symmetric positive definite, ensuring the derived source properties have physically meaningful values. The framework accounts for the autocorrelation structure of the errors and incorporates hyperpriors on the uncertainty. We validate this methodology using a synthetic test and subsequently apply it to the 2019 M_w7.1 Ridgecrest earthquake using teleseismic data. The distributions of second moments determined for this event provide probabilistic descriptions of low-dimensional rupture characteristics that are generally consistent with results from previous studies. The success of this case study suggests that probabilistic and comparable finite source properties may be discerned for large global events regardless of the quality and coverage of local instrumentation.

Plain Language Summary

Earthquake science is presented with the challenging problem of determining properties of earthquake sources that occur deep within the Earth using observations made at the surface of the Earth. Typically, the process for determining these important quantities involves finding solutions to complicated optimization problems that, given the necessarily poor data coverage, are poorly constrained. With this challenge in mind, we present a framework to solve for some fundamental properties of earthquake sources like spatial extent, rupture propagation direction, and duration. This approach requires few assumptions about the geometry of the fault that ruptured and the dynamics of the rupture process, in contrast to more traditional methods. This procedure also provides a probabilistic description of these earthquake source properties, which is essential, because the uncertainty inherent to this problem dictates that we cannot confidently choose any one particular solution. We demonstrate this method's utility by applying it to the 2019 magnitude 7.1 Ridgecrest earthquake. Through this application, we show that this framework can yield probabilistic and comparable estimations of rupture properties for large global earthquakes using seismic data recorded at great distances.

1 Introduction

Earthquakes are known to exhibit complex rupture processes that vary strongly in space and time. A better understanding of the factors controlling earthquake behavior consequently requires constraining the finite source properties of earthquakes. Today, high dimensional estimates ($\sim$ 1000 parameters) of finite source properties are routinely computed for significant earthquakes (e.g. Wald & Heaton, 1992; Ammon, 2005; Moreno et al., 2010; Ide et al., 2011; Ross et al., 2019). These estimates usually involve the inversion for slip on a predefined fault plane using some combination of seismic, geodetic, and tsunami data with kinematic constraints placed on the rupture propagation (Hartzell & Heaton, 1983; Du et al., 1992; Saito et al., 2011). These solutions, termed finite-fault slip distributions, provide a detailed image of time-dependent slip behavior during an earthquake rupture. However, these inversions require often arbitrary parameterization of the source geometry, have a general lack of sensitivity to rupture velocity, and need substantial regularization due to the non-uniqueness of the inverse problem (e.g. Lay, 2018; Wang et al., 2020). This nonuniqueness presents challenges to objectively comparing finite source properties between events, and thus limits our ability to discern patterns in earthquake behavior that could inform a deeper understanding of earthquake phenomenology.

The limitations of routinely computed estimates of finite source properties motivates the development of alternative estimates that overcome these limitations. One potential alternative is the second moment formulation (G. Backus & Mulcahy, 1976a, 1976b), in which higher-order mathematical moments of the stress glut, a source representational quantity, are used to describe basic properties of the rupture process in space and time. Higher-order stress glut moments have been successfully computed in the past (Bukchin, 1995; McGuire et al., 2000, 2001; McGuire, 2002, 2004; Chen, 2005; Meng et al., 2020), but this methodology has received little attention compared to slip inversions. The second-moment formulation yields low-dimensional, physically-motivated estimates of the spatial extent, directivity, and duration of earthquake ruptures. It requires no prior knowledge of the rupture velocity, and makes only mild assumptions about the source geometry. Being free of gridding and associated discretization issues that complicate slip inversions, the second moment formulation can more objectively facilitate comparisons between events, helping to find common patterns. Illuminating these patterns may help address outstanding questions in earthquake science relating to how fault zones may facilitate or impede earthquake ruptures.

In this study, we use the well-studied 2019 M_w7.1 Ridgecrest earthquake as a vehicle to demonstrate our methodology (e.g. Ross et al., 2019; Barnhart et al., 2019). The wealth of high quality geodetic data and dense seismic instrumentation have been incorporated into numerous finite-fault slip distribution models (Ross et al., 2019; Barnhart et al., 2019; Liu et al., 2019; Xu et al., 2020; Goldberg et al., 2020; Wang et al., 2020; Jin & Fialko, 2020; Yue et al., 2021). Additionally, rapid field response studies have provided high resolution characterizations of the surface fault rupture and displacement (Ponti et al., 2020; DuRoss et al., 2020). Further, other source estimation techniques such as subevent inversion (Jia et al., 2020) and multi-array backprojection (Xie et al., 2021) have yielded additional constraints on the time-dependence of moment release during the mainshock.

Our contributions in this paper are as follows. We develop a Bayesian inverse scheme for second moments using teleseismic data. We employ Hamiltonian Monte Carlo sampling and automatic differentiation to efficiently sample from the posterior distribution. In doing so, we apply a set of transformations that ensure positive definiteness of the second moments. We demonstrate the efficacy of our methodology by applying the inversion scheme to the Ridgecrest mainshock. We show that our methodology is useful for determining probabilistic and comparable descriptions of low-dimensional rupture parameters with few a priori assumptions.

2 Preliminaries

Because an earthquake is constituted by a localized zone of inelastic deformation, we can represent the source region as a localized departure from elasticity. These departures can be quantified using the so-called stress glut, $\mathbf{\Gamma}$, the tensor field computed by applying an idealized Hooke's law to the inelastic component of strain in a system (G. Backus & Mulcahy, 1976a, 1976b). The stress glut is nonzero only within the source region. The stress glut is a complete representation of a seismic source in space and time that can be used to reproduce displacements everywhere on Earth for an arbitrary source (Dahlen & Tromp, 1998). Given the typically sparse distribution of seismic observations, solving for the full stress glut is an ill-posed problem. We can simplify the stress glut by assuming the source geometry is constant in space and time:

$$\Gamma_{ij}(\boldsymbol{\xi}, \tau) = \hat{M}_{ij} f(\boldsymbol{\xi}, \tau) \tag{1}$$

Where is $\hat{\mathbf{M}}$ is the normalized mean seismic moment tensor and f is the scalar function defined at the position $\boldsymbol{\xi}$ and time τ. This approximation reduces the solution from a tensor field to a scalar field and is most valid for seismic sources with stable source mechanisms.

We can further reduce the dimensionality of the stress glut by first recognizing that any scalar function in a bounded interval may be uniquely determined by its collection of polynomial moments. Because f captures a static displacement, f is nonzero for infinite time and thus occupies an unbounded interval, but $\dot{f}$ vanishes to zero at the cessation of rupture and is thus captured within a bounded interval. Hence, considering that the stress glut prescribes displacements due to an arbitrary seismic source, we can represent seismic displacements as the superposition of the spatiotemporal moments of the rate function $\dot{f}$. We represent the spatial and temporal components of these moments separately, with spatial order m and temporal order n. At low frequencies, we can truncate this infinite series such that we only include terms with moments of order $m+n \leq 2$. We can then explicitly define the measured displacements for a station i at low frequencies as:

$$\begin{aligned} u_i(\mathbf{r}, t) \quad = \quad & \dot{f}^{(0,0)}(\boldsymbol{\xi^c}, \tau^c) \hat{M}_{jl} \frac{d}{d\xi_l} \int_{-\infty}^{+\infty} G_{ij}(\boldsymbol{\xi^c}, \tau^c, \mathbf{r}, t) dt \\ & - \dot{f}_x^{(1,1)}(\boldsymbol{\xi^c}, \tau^c) \hat{M}_{jl} \frac{d}{d\xi_x} \frac{d}{d\xi_l} G_{ij}(\boldsymbol{\xi}_c, \tau^c, \mathbf{r}, t) \\ & + \frac{1}{2} \dot{f}_{xy}^{(2,0)}(\boldsymbol{\xi^c}, \tau^c) \hat{M}_{jl} \frac{d}{d\xi_x} \frac{d}{d\xi_y} \frac{d}{d\xi_l} \int_{-\infty}^{+\infty} G_{ij}(\boldsymbol{\xi^c}, \tau^c, \mathbf{r}, t) dt \\ & + \frac{1}{2} \dot{f}^{(0,2)}(\boldsymbol{\xi^c}, \tau^c) \hat{M}_{jl} \frac{d}{d\xi_l} \frac{d}{dt} G_{ij}(\boldsymbol{\xi^c}, \tau^c, \mathbf{r}, t) \end{aligned} \tag{2}$$

Where $\mathbf{G}$ is a Green's tensor prescribing the path effects from a source with the centroid location $\boldsymbol{\xi^c}$ and centroid time τ^c to an arbitrary station with the location $\mathbf{r}$ at time t, and $\dot{f}^{(m,n)}(\boldsymbol{\xi^c}, \tau^c)$ is the moment of the scalar rate function $\dot{f}(\boldsymbol{\xi}, \tau)$ of spatial order m and temporal order n taken about the source centroid in space and time (Bukchin, 1995). Equation 2 is only valid at low-enough frequencies, and the determination of "low-enough" depends on the spatiotemporal dimensions of the source.

Several of the moments are of routine use in seismology, while the rest are worked with sparingly. The moment of order $m+n=0$ is the scalar moment of the source. The moments of order $m+n=1$ correspond to the spatial ($m=1$) and temporal ($n=1$) centroids of the source. Perhaps unfamiliar are the moments of order $m+n=2$; these moments describe low-dimensional finite properties of earthquake sources. In particular, $\dot{f}^{(2,0)}(\boldsymbol{\xi^c}, \tau^c)$ is the spatial covariance of the stress glut, $\dot{f}^{(1,1)}(\boldsymbol{\xi^c}, \tau^c)$ is the spatiotemporal covariance of the stress glut, and $\dot{f}^{(0,2)}(\boldsymbol{\xi^c}, \tau^c)$ is the temporal variance of the stress glut. These so-called second moments yield low-dimensional, physically-motivated approximations of the source volume, source directivity, and source duration respectively (G. E. Backus, 1977).

To understand the physical significance of these second moments, we emphasize that the spatial second moments and the temporal second moments are covariances and variances respectively. From these quantities we can thus obtain the standard deviation of the stress-glut distribution, and the standard deviation is a measure of the width of the distribution. We can then define characteristic dimensions of the source using standard deviations of the stress glut derived from the second moments (G. E. Backus, 1977; Silver & Jordan, 1983). These characteristic dimensions may be defined using a metric of ± 1 standard deviation from the centroid:

$$r^c(\hat{\mathbf{n}}) = \sqrt{\hat{\mathbf{n}}^{\mathbf{T}} \cdot [\dot{f}^{(2,0)}(\boldsymbol{\xi}^{\boldsymbol{c}}, \tau^c)/\dot{f}^{(0,0)}(\boldsymbol{\xi}^{\boldsymbol{c}}, \tau^c)] \cdot \hat{\mathbf{n}}},$$

$$t^c = 2\sqrt{\dot{f}^{(0,2)}(\boldsymbol{\xi}^{\boldsymbol{c}}, \tau^c)/\dot{f}^{(0,0)}(\boldsymbol{\xi}^{\boldsymbol{c}}, \tau^c)}, \tag{3}$$

Where $r^c(\hat{\mathbf{n}})$ is the extent of the characteristic volume from the centroid in the direction of arbitrary unit vector $\hat{\mathbf{n}}$ and t^c is the characteristic duration of the source. We'll also define a characteristic length of the source, L^c, as $2 \cdot r^c(\boldsymbol{\eta})$, where $\boldsymbol{\eta}$ is the principal eigenvector of $\dot{f}^{(2,0)}(\boldsymbol{\xi}^{\boldsymbol{c}}, \tau^c)$. Using the mixed second moments and the characteristic dimensions described in equation 3, we can get estimates of the velocity of the rupture:

$$\mathbf{v_0} = \dot{f}^{(1,1)}(\boldsymbol{\xi}^{\boldsymbol{c}}, \tau^c)/\dot{f}^{(0,2)}(\boldsymbol{\xi}^{\boldsymbol{c}}, \tau^c),$$

$$v^u = L^c/t^c \tag{4}$$

Where $\mathbf{v_0}$ is the average instantaneous velocity of the centroid of the rupture and v^u is an upper bound on the average velocity of the rupture. The quantities described in equations 3 and 4 thus yield physically interpretable values with which we can evaluate and compare stress glut second moment solutions and contextualize these solutions in the broader source characterization literature.

3 Methods

3.1 Data and Preprocessing

In this study we work with both real and synthetic seismic waveform data. The real data are vertical component seismic data from 48 Global Seismographic Network (GSN) stations (Figure 1). We selected these stations both by the source-to-receiver distance and by evaluating how well the waveforms were approximated by point source synthetics computed using the gCMT solution. The seismograms used in the inversion are 700 second windows about the surface wave packet that we manually selected from 7200 second windows that start at the gCMT centroid time for the Ridgecrest mainshock. In this study, we only use the vertical component of the seismograms and only include R1 arrivals. The addition of other phases like G1 arrivals and body waves, as well as R2 and G2 arrivals, would further constrain the posterior distribution, but we reserve the inclusion of these additional phases for future studies. We down-sample the waveform data to a 0.05 Hz sampling rate, which reduces the correlation between samples and minimizes the computational demands of the inversion. As part of the construction of the forward propagation matrix, we computed the Green's tensor using the gCMT moment tensor and centroid location, which we perturbed to compute the requisite spatial derivatives numerically.

To compute the Green's tensor, we use the 3D Earth model S362ANI + M (Moulik & Ekström, 2014) and the full waveform modeling software Salvus (Afanasiev et al., 2019), which employs the spectral element method to simulate wave propagation. After computing

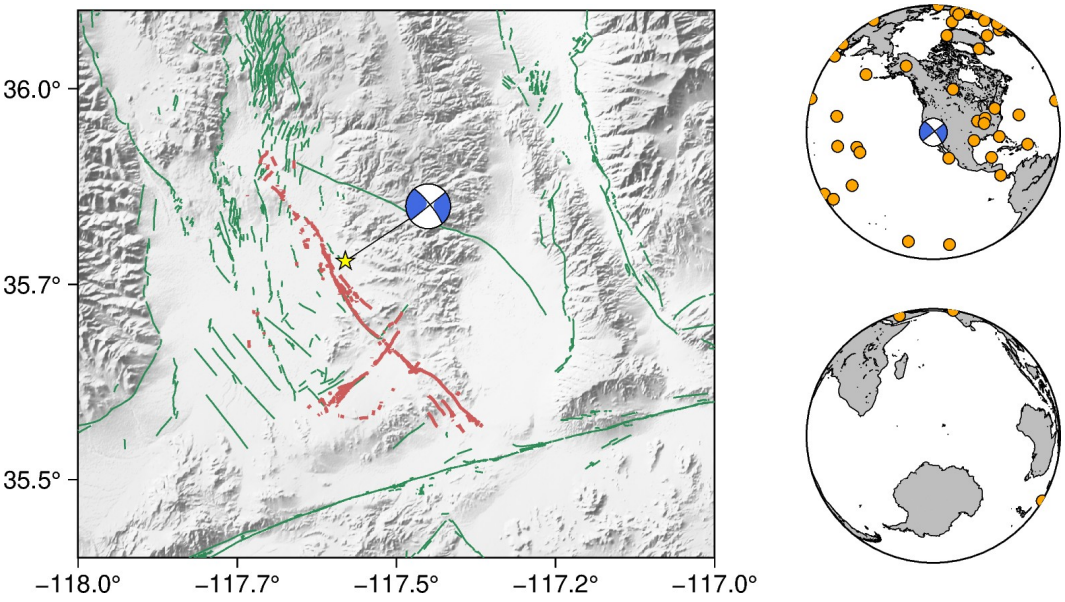

Figure 1. Left: Geographic setting of the 2019 Ridgecrest Sequence. Focal mechanism is the gCMT solution for the sequence mainshock. Yellow star indicates the gCMT solution centroid position. Green and red lines indicate USGS mapped quaternary faults (USGS & CGS, 2021) and faults that were activated during the Ridgecrest Earthquake sequence (Ross et al., 2019). The strike, dip, and rake of the true nodal plane as given by the gCMT solution are 321°, 81°, and 180° respectively. Map coloring is reflective of elevation. Right: Global distribution of stations from which waveforms were used in this study.

this Green's tensor, we initially keep these waveforms at a high frequency (4 Hz) to improve numerical stability when approximating integrals and derivatives. We take the necessary temporal and spatial derivatives and integrals of this Green's tensor numerically using a centered finite difference approximation. For the spatial derivatives, we tested numerous finite difference offsets from the spatial centroid using synthetic tests, which are described subsequently. Given these tests, we prefer a perturbation distance of 250 m because this distance is both small enough to yield a reasonable approximation of the spatial derivative and large enough to be numerically stable. The construction of the forward propagation matrix, which we describe subsequently, requires both the gCMT moment tensor and the Green's tensor derivatives and integrals.

A particularly important step in the preprocessing of these waveforms is selecting which frequency band to use in the inversion. There are two key issues that need to be balanced when making this determination. Firstly, equation 2 is a low frequency approximation; at higher frequencies, moments of order $m + n > 2$ become more significant. This means that the frequency band needs to be low enough such that we exclude moments of order $m+n > 2$, or else the inversion will be biased by these higher-order terms. Secondly, moments of order $m + n = 0$ and $m + n = 1$ are used. The values used for these lower-order terms are robust, but are subject to error. Thus, we need to ensure that the contributions from moments of order $m + n = 2$ are large enough such that they exceed the magnitude of error of the lower order terms, otherwise the inversion will be dominated by this error. In short, the frequency band should be high enough such that the contribution of the second moments markedly exceeds the error on the solutions for the zeroth and first moments, and be low enough such that the contribution of the third moments is reasonably small. A good metric by which to make this selection is to use the observation that the contribution of moments of order $m+n$

is approximately proportional to $(D/P)^{m+n}$ (assuming $(D/P) < 1$) where D is the source duration and P is the period (G. E. Backus, 1977). Looking at the distribution of scalar moment estimations for the Ridgecrest mainshock obtained using teleseismic data (GCMT, 2019; USGS, 2019; Liu et al., 2019), we likely approach the order of the error on the zeroth moment when the contribution of the second moments exceeds 5% of the zeroth moment. To obtain a period band where the second moments are significant compared to the error on the lower-order terms and the contribution of the higher-order terms are always small compared to the second moments, we select a period band that obeys both $(D/P)^2 > 0.05$ and $(D/P)^3 < 0.05$. Taking 25 s as an approximate source duration for the Ridgecrest mainshock, this yields a period band of 70-110 s. Since source durations are routinely estimated for global events (e.g. Vallée & Douet, 2016), this method of frequency-band selection is applicable to most other global events.

We only use stations in the distance range $10 - 90°$, with the exception of a few stations with exceptional fits at distances just above 90° (see Figure 1), to minimize the bias imposed by the integrated effect of Earth model error. We then align the Green's tensor and observed displacements of the remaining stations via cross correlation and select a 700 s window that encompasses the surface wave packets at each station. The time shifts, which are intended to correct for time errors due to variable Earth model inaccuracy, are performed at a frequency band at which the third moments are small. There is thus assumed to be minimal skewness in the source time function, and we then expect the cross-correlation to account for the Earth-model effected timing error without misaligning the centroid time. We apply a Hamming taper to the surface wave packet to minimize the contributions of signal at the start and end of the time window. These time windows constitute the time-segments of the Green's tensor and data. Because the contribution of moments of order $m + n = 2$ should still be relatively small in the selected frequency band, the synthetic waveforms produced using a point source approximation should be similar to the observed waveforms. We thus perform an additional manual quality control of the remaining stations, and we remove stations that show a poor match between the data and the point source waveforms. Both the waveforms that were kept and the waveforms that were thrown out in the course of this quality control are shown in Figure S1.

Before applying this methodology to real data, we will show a test of the outlined inversion procedure using a synthetic source. For this test, we prescribe a 55x15 km rectangular fault with a strike and dip corresponding to the nodal plane of the gCMT solution associated with the true rupture surface. We then define a grid of point sources, each with the gCMT source mechanism and equal fraction of the gCMT moment, along this prescribed fault such that the spatial release of moment can be approximated as uniform distributions of moment release along the strike and dip of the fault. We delay the activation of these point sources according to a prescribed rupture velocity of 2.5 km/s along strike, resulting in an event duration of 22 s, such that the moment release with time can also be approximated as a uniform distribution. Using the fact that the width of a uniform distribution is equal to $2\sqrt{3}\sigma$, where σ is the standard deviation of the Gaussian approximation of that uniform distribution, we can determine the true second moment solution for this synthetic source.

3.2 Inversion

Equation 2 describes the forward model for a second moment tensor source. While it appears unruly, many of the terms that constitute it are easily accessible. For a given source, we can observe $u_i(\mathbf{r}, t)$ using seismic instrumentation; we can solve for $\mathbf{G}$, $\mathbf{M}$, and $(\boldsymbol{\xi^c}, \tau^c)$ using routine techniques; and we can compute the necessary derivatives and integrals using numerical methods. Thus, in equation 2, only the moments of the scalar function $\dot{f}$ are unknown. We can then pose equation 2 as a linear inverse problem:

$$\mathbf{d} = \mathbf{F}\mathbf{p} \tag{5}$$

where $\mathbf{d}$ is a vector of measured displacements, $\mathbf{F}$ is a forward propagation matrix of spatial and temporal integrals and derivatives of $\mathbf{G}$, the columns of which are weighted by the components of $\mathbf{M}$, and $\mathbf{p}$ is a vector of parameters which constitute the lower-order moments of the stress glut.

Numerous Bayesian methods for source parameter inversion have been proposed for problems such as focal mechanism estimation (Wéber, 2006; Walsh et al., 2009; Lee et al., 2011; Duputel et al., 2014) and finite-fault slip distribution estimation (Monelli et al., 2009; Minson et al., 2013). Bayesian inference has been growing increasingly popular because it provides an ensemble of solutions that are informed by both data and prior distributions determined by physical constraints or ground truth. The Bayesian formulation described here allows for the computation of an ensemble of second moment solutions, with each providing a low dimensional estimate of the source process.

The posterior distribution for this problem can be written as follows (e.g. Tarantola, 2005),

$$p(\mathbf{p}, \sigma|\mathbf{d}) \propto p(\mathbf{d}|\sigma, \mathbf{p})\; p(\sigma)\; p(\mathbf{p}), \tag{6}$$

where σ is a hyperparameter. For the likelihood term, $p(\mathbf{d}|\sigma, \mathbf{p})$, we use a multivariate normal distribution,

$$p(\mathbf{d}|\sigma, \mathbf{p}) \propto \frac{1}{\sqrt{|\Sigma|}} \exp(-\frac{1}{2}(\mathbf{d} - \mathbf{Fp})^{\mathrm{T}}\, \mathbf{\Sigma}^{-1}\, (\mathbf{d} - \mathbf{Fp})) \tag{7}$$

Since the observations are time-series data, errors in the forward model will be subject to temporal autocorrelation. We can account for this correlation structure through the data covariance matrix, $\mathbf{\Sigma}$, as outlined in (Duputel et al., 2014). If d_i and d_j are measured displacements that are on the same trace and are recorded by the same station:

$$\Sigma_{ij} = \sigma \cdot \exp(-|i - j|\delta t/\Delta t) \tag{8}$$

Where σ is the hyperparameter included in equations 6 and 7, δt is the sampling rate, and Δt is the period of the shortest period information included in the time-series. This prescribes a block diagonal matrix where the blocks have the same length as the time windows taken from each station. This correlation structure accounts for temporal correlation in the errors, but not any spatial correlation. In this paper we assume that the observations are spatially distributed sparsely enough that spatially-correlated errors are negligible.

We use uninformed priors in this case study, but note that informed priors can easily be incorporated (Gelman et al., 2010). That is, with the physical interpretation of the second moment properties that we will describe shortly, priors on the spatial extent, directivity, and duration may be imposed given observational ground truth. For example, if the true nodal plane of an earthquake is known, Gaussian priors may be placed on the spatial second moment parameters to restrict the principal eigenvector of the spatial covariance matrix to abut the true nodal plane.

The total number of parameters in this inverse problem is 11, and we approximate $p(\mathbf{p}, \sigma|\mathbf{d})$ using Markov Chain Monte Carlo (MCMC) sampling to obtain an ensemble of solutions. We do not solve for the zeroth or first order moments, and instead use the gCMT solution as our moment tensor and centroid location. Future work will focus on jointly solving for the lower order moments together with the second moments. As the parameter space is too large for efficient inference with standard Metropolis-Hastings type samplers, we instead sample from the posterior distribution using Hamiltonian Monte Carlo (HMC) sampling (Neal, 2010), which is an instance of the Metropolis-Hastings algorithm that can efficiently sample large parameter spaces using principles from Hamiltonian dynamics. This is accomplished in part by incorporating gradient information into the sampling process;

however, it requires a means to also compute gradients efficiently. Here, we accomplish this through the use of reverse-mode automatic differentiation (Innes, 2019).

For each Markov chain in the inversion, we draw 5000 samples from the posterior distributions after drawing 5000 burn-in samples. The momentum distribution has a diagonal mass matrix and the samples are updated using an ordinary leapfrog integrator (Neal, 2010). To evaluate convergence, we run at least 3 chains of the inversion and compute the Gelman-Rubin diagnostic using the computed set of chains (Gelman & Rubin, 1992). That is, we compare the variability within chains to the variability between chains to determine if the chains all converge to the same target distributions.

Additionally, as described in prior work on this subject (Bukchin, 1995; McGuire et al., 2001), the second moments of the stress glut are covariances, and therefore only a subset of the parameter space produces valid solutions. Specifically, the second moments are symmetric positive definite,

$$\mathbf{X} = \begin{bmatrix} \dot{f}^{(2,0)}(\boldsymbol{\xi}^{\boldsymbol{c}}, \tau^c) & \dot{f}^{(1,1)}(\boldsymbol{\xi}^{\boldsymbol{c}}, \tau^c) \\ \dot{f}^{(1,1)}(\boldsymbol{\xi}^{\boldsymbol{c}}, \tau^c)^T & \dot{f}^{(0,2)}(\boldsymbol{\xi}^{\boldsymbol{c}}, \tau^c) \end{bmatrix} \succeq 0. \tag{9}$$

Physically, this is equivalent to saying that the spatial extent and duration of the source are both non-negative. Typically, when performing a constrained Bayesian inversion, the easiest course of action is to sample under an unconstrained parameter space and subsequently transform those parameters into the necessarily constrained parameter space (Gelman et al., 2010). To this end, we note that, by the Cholesky Factorization Theorem, every symmetric positive-definite matrix can be decomposed into the product of some lower triangular matrix with a positive diagonal and the transpose of that same lower triangular matrix. This means that given $\mathbf{X}$, there exists a lower triangular matrix $\mathbf{L}$ with positive diagonal components such that:

$$\mathbf{X} = \mathbf{L}\mathbf{L}^T \tag{10}$$

Thus, we can sample freely from the unconstrained off-diagonal components of $\mathbf{L}$ and from the natural logarithm of the diagonal components of $\mathbf{L}$. Then, to evaluate our sample against our data, we can simply build $\mathbf{L}$ using our sample components and then construct $\mathbf{X}$ using equation 10. From $\mathbf{X}$ we can extract a valid $\mathbf{p}$ with which we evaluate the likelihood of our sample. A keen observer may notice that while $\mathbf{X}$ need only be symmetric positive semi-definite, the Cholesky factorization forces $\mathbf{X}$ to be positive definite. In practice, this distinction is inconsequential, as a positive semi-definite $\mathbf{X}$ suggests that at least one dimension of the source is identically zero, which will never be true in reality.

4 Results

We first perform our inversion on the synthetic test described in the Methods section. In the interest of evaluating the resolvability of parameters for the Ridgecrest mainshock, we invert for these second moments using the same distribution of stations and the same windowing procedure that we use for the real event. For this test, we also use the mean σ from the to-be-described inversion of real data so we can test this inversion in the presence of realistic error. The marginal probability distributions for each parameter and the joint probability distributions for each pair of parameters are shown in Figure 4. These plots show that most of the parameters are either uncorrelated or weakly correlated with each other, with the exception of some weak correlation between some closely-related spatial variables and some spatial variables with the temporal variable. These plots also show that almost all the components of the expected second moment covariance matrix fall well within the ensemble of solutions, with the exception of a slight underestimate of the magnitude of the north component of the mixed second moment. This discrepancy may be due to the imperfect assumption of uniform moment release with time for this test due to the discretization of the source.

We can further test the fidelity of our inversion results by computing synthetic waveforms using equation 2 and evaluating the fit to the observed waveforms generated for this synthetic example. The waveforms for an ensemble of second moment solutions from a single chain for the synthetic test are shown for a subset of stations with a large diversity of azimuths and distances in Figure 3. The waveform fits match the synthetic observations very well, particularly when the full ensemble of solutions is considered. As is shown in this figure, the inclusion of the inverted-for second moments of the stress glut perturb the point-source waveforms to fit the synthetic observations, thus successfully accounting for the finiteness of the source.

In order to represent the second moment solutions for the synthetic test in a more physically interpretable way, we convert the ensembles of second moments into ensembles of L^c, t^c, $|\mathbf{v_0}|$, and v^u. Additionally, because the directions associated with L^c and $|\mathbf{v_0}|$ are important, we consider the strike (θ) and plunge (ϕ) associated with these quantities as well. We plot the ensembles of these quantities in Figure 4. We find that the ensembles of these converted parameters are largely normally distributed, and the values associated with the anticipated solution for the synthetic test all fall within these ensembles.

Now, we invert for the second moments of the 2019 Ridgecrest mainshock using the real data. The distributions of the 10 independent parameters of the second moments for a single chain of the inversion using the real data are shown in Figure 5. We run the inversion for a set of chains, shown in Figure S2, and compute the Gelman-Rubin diagnostic (Gelman & Rubin, 1992) using these chains. The Gelman-Rubin values are far less than 1.1, suggesting that the chains have converged to the target posterior distributions for the second moments. The joint probability distributions for each pair of parameters are shown in Figure 5. As with the synthetic test, these joint distributions show that the inverted parameters are mostly uncorrelated with each other. Some of the marginal distributions of the second moments are skewed due to the positive-definite constraint placed on the inversion. The distribution for the hyperparameter σ is shown in Figure S3. We can also evaluate the waveform fits for the inversion using real data. A representative subset of these waveform fits is shown in Figure 6. The computed waveforms for the ensemble of solutions inverted for under this framework fit the observed waveforms reasonably well.

Using these ensembles of second moments, we can summarize the physical parameters of the Ridgecrest mainshock. We show these distributions in Figure 7. As with the synthetic test, most of these ensembles are normally distributed, with the exception of ϕ^{L^c}, which is bimodal, which reflects some nonlinearity in the mapping between the raw second moments and the derived parameters. We find that, within two standard deviations, the characteristic length of the rupture is 47.3 ± 6.0 km with strike and plunge of $327.7 \pm 7.5^\circ$ and $-0.2 \pm 9.1^\circ$

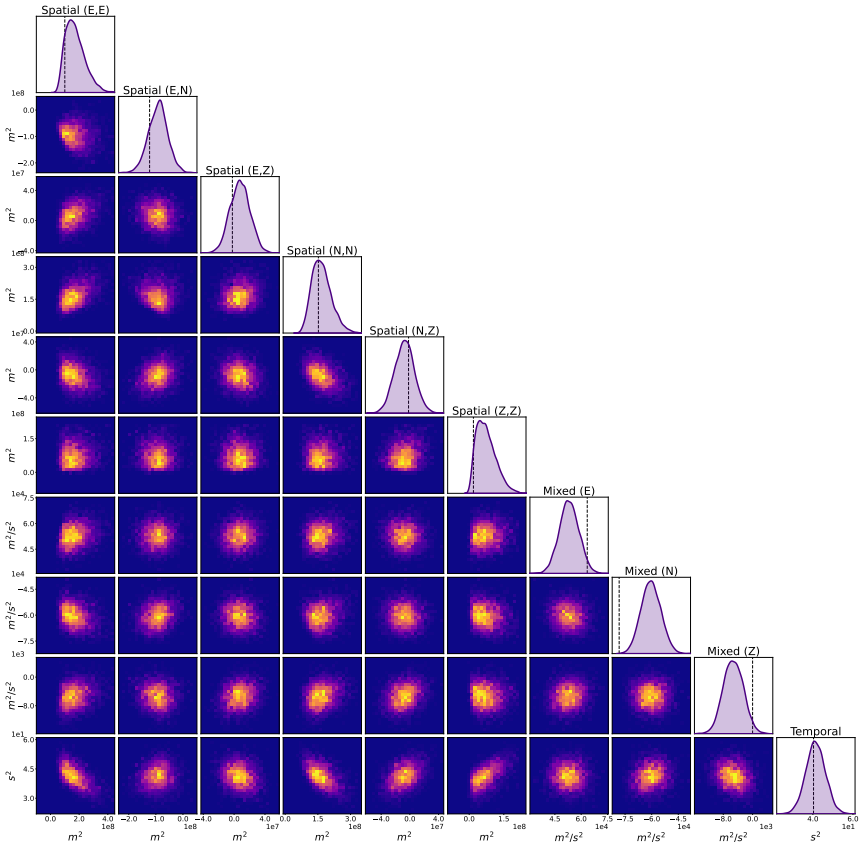

Figure 2. Marginal and joint probability density plots for the 10 independent parameters inverted for the synthetic test in this study. Off-diagonal plots are 2-dimensional histogram plots representing the joint probability distribution for each pair of independent parameters. On-diagonal plots are kernel density estimate plots for the marginal distributions of the adjacent joint probability distributions. Black dotted lines indicated the anticipated solution for each parameter in the inversion.

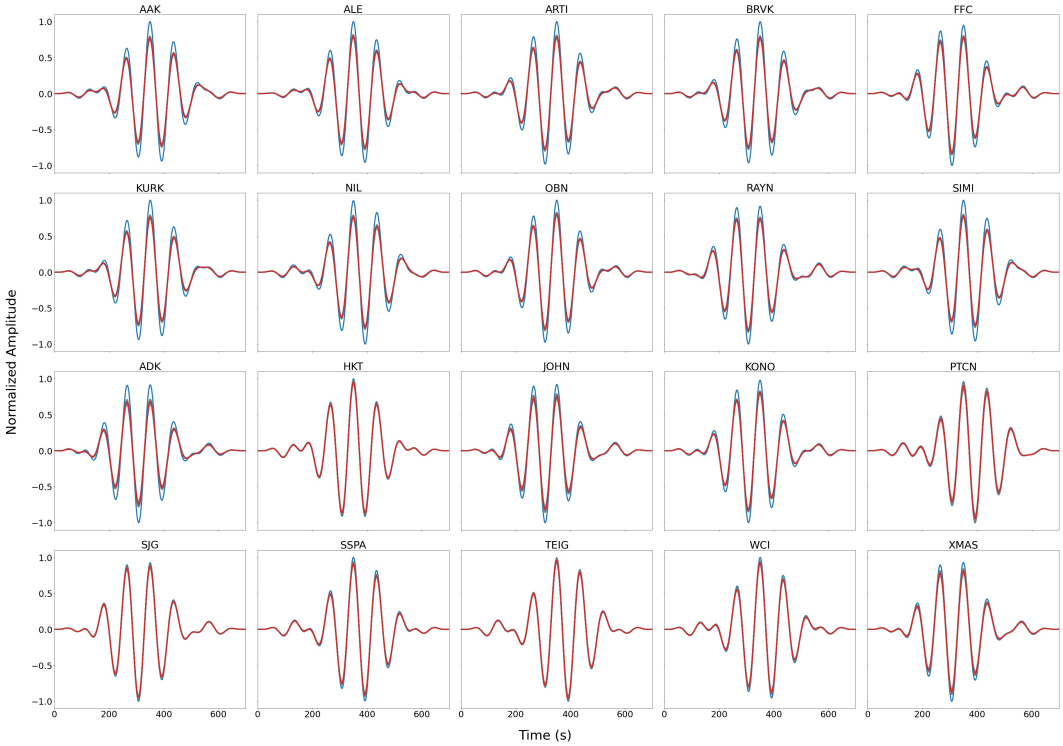

Figure 3. Waveform fits for a large subset of the windowed waveforms for the synthetic test conducted in this study. Waveforms are labeled according to the GSN station at which they were generated. Black waveforms are synthetic observations. Gray waveforms are generated using a single solution from the ensemble of solutions from our inversion. Waveforms from each solution in the ensemble are plotted. Red waveforms are generated using the mean solution of the ensemble of solutions from our inversion. Blue waveforms are generated using only the gCMT solution and exclude any consideration of the second moments of the stress glut.

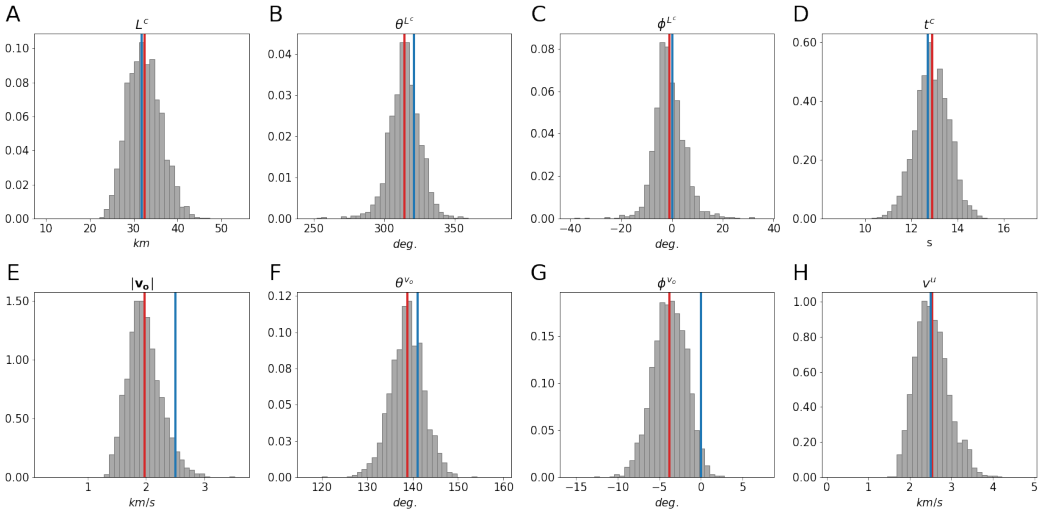

Figure 4. Physically motivated representations of the ensembles of second moment solutions for the synthetic test. A. characteristic length (L^c), B. characteristic length strike (θ^{L^c}), C. characteristic length plunge (ϕ^{L^c}), D. characteristic duration (t^c), E. instantaneous centroid velocity magnitude ($|\mathbf{v_0}|$), F. instantaneous centroid velocity strike ($\theta^{\mathbf{v_0}}$), G. instantaneous centroid velocity plunge ($\phi^{\mathbf{v_0}}$), H. average velocity upper bound (v^u). Histogram shows density of realizations in the ensemble. Red vertical line shows the mean realization. Blue line shows the anticipated realization.

respectively. The characteristic duration of the rupture is 14.5 ± 1.1 s. The instantaneous centroid velocity of the Ridgecrest mainshock has a magnitude of 1.3 ± 0.3 km/s with strike and plunge of $127.4 \pm 9.9°$ and $1.3 \pm 4.8°$ respectively. Finally, the average velocity upper bound is 3.3 ± 0.6 km/s. We summarize the results for the spatial and mixed second moments by plotting projections of ellipsoids defined using $r^c(\hat{\mathbf{n}})$ from equation 3, which yield descriptions of the volume in which most of the moment of the source was released, and $\mathbf{v_0}$ for a subset of 500 solutions from our ensemble of second moment solutions for this source in Figure 8.

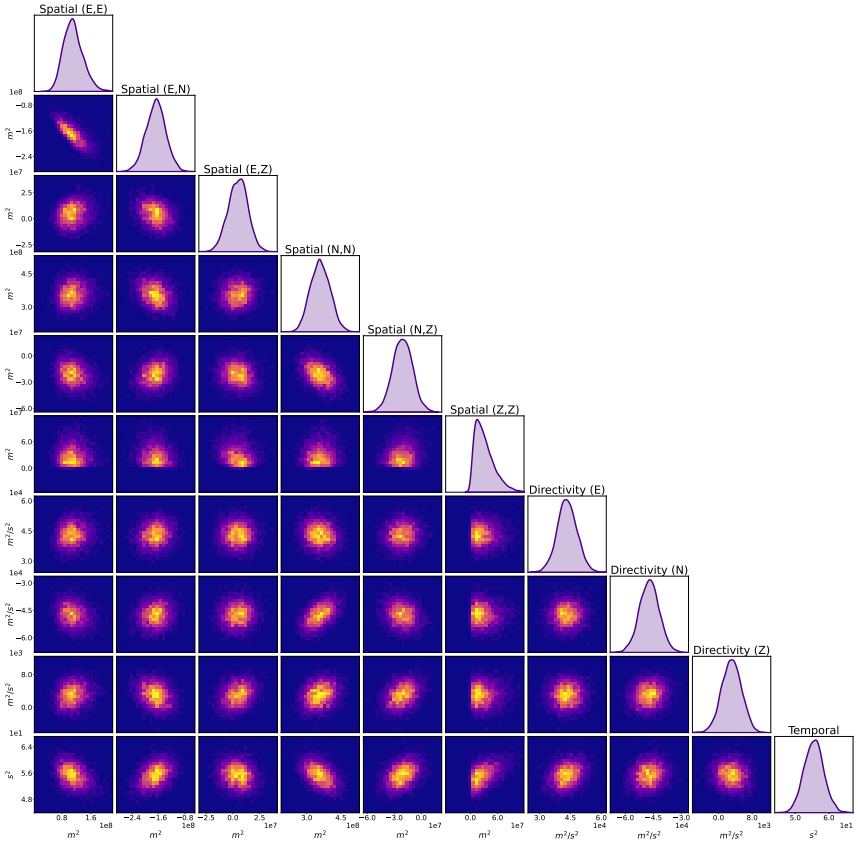

Figure 5. Marginal and joint probability density plots for the 10 independent parameters inverted for in this study. Off-diagonal plots are 2-dimensional histogram plots representing the joint probability distribution for each pair of independent parameters. On-diagonal plots are kernel density estimate plots for the marginal distributions of the adjacent joint probability distributions.

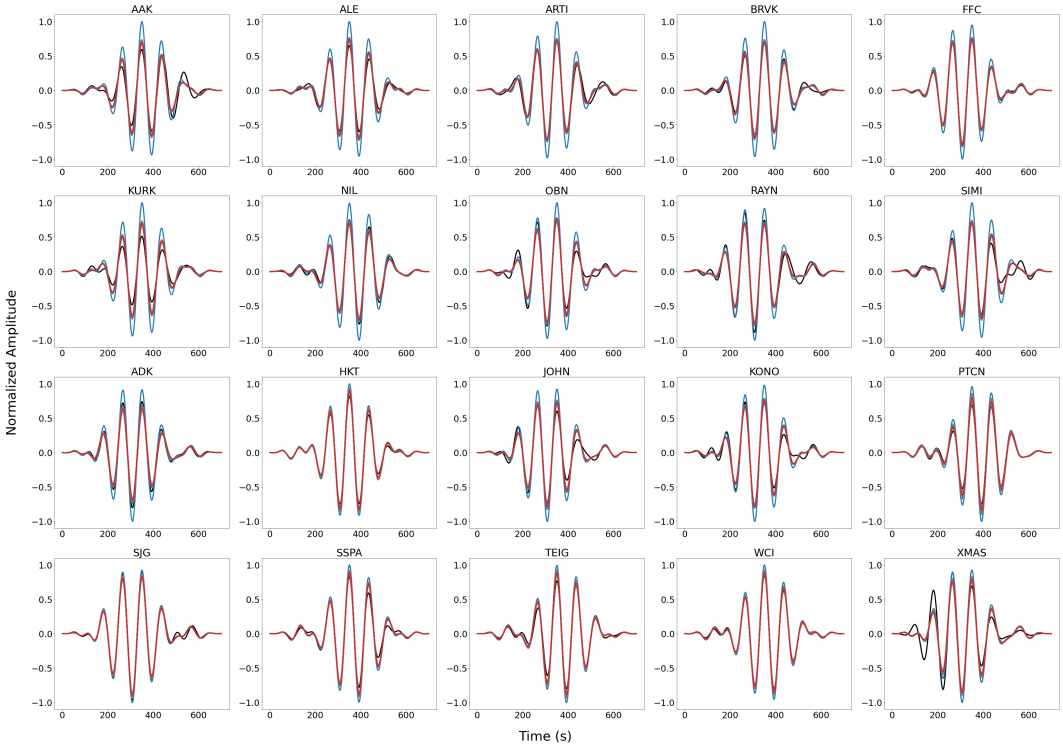

Figure 6. Waveform fits for a subset of the windowed waveforms used in this study. Waveforms are labeled according to the GSN station at which they were recorded. Black waveforms are observations. Gray waveforms are generated using a single solution from the ensemble of solutions from our inversion. Waveforms from each solution in the ensemble are plotted. Red waveforms are generated using the mean solution of the ensemble of solutions from our inversion. Blue waveforms are generated using only the gCMT solution and exclude any consideration of the second moments of the stress glut.

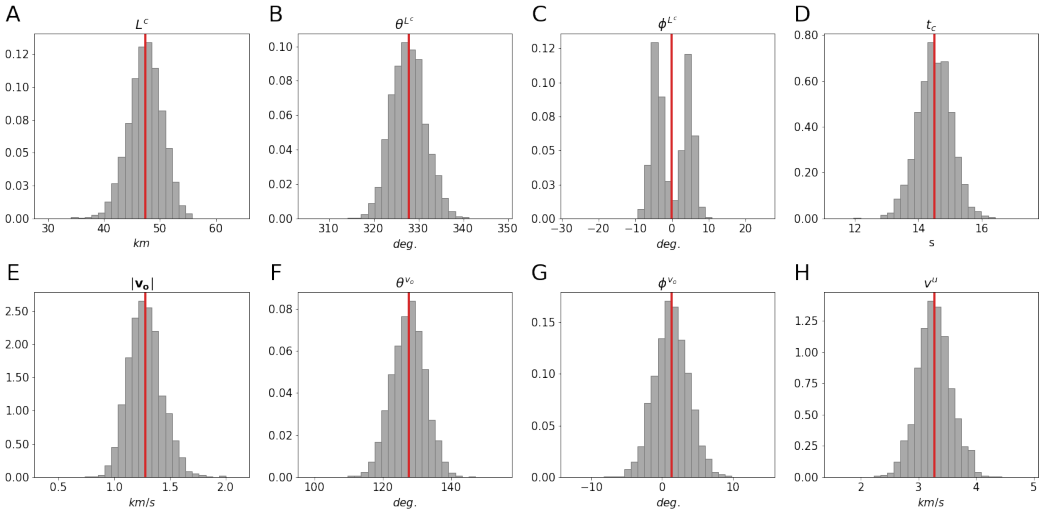

Figure 7. Physically motivated representations of the ensembles of second moment solutions for the 2019 Ridgecrest mainshock. A. characteristic length (L^c), B. characteristic length strike (θ^{L^c}), C. characteristic length plunge (ϕ^{L^c}), D. characteristic duration (t^c), E. instantaneous centroid velocity magnitude ($|\mathbf{v_0}|$), F. instantaneous centroid velocity strike ($\theta^{\mathbf{vo}}$), G. instantaneous centroid velocity plunge ($\phi^{\mathbf{vo}}$), H. average velocity upper bound (v^u). Histogram shows density of realizations in the ensemble. Red vertical line shows the mean realization.

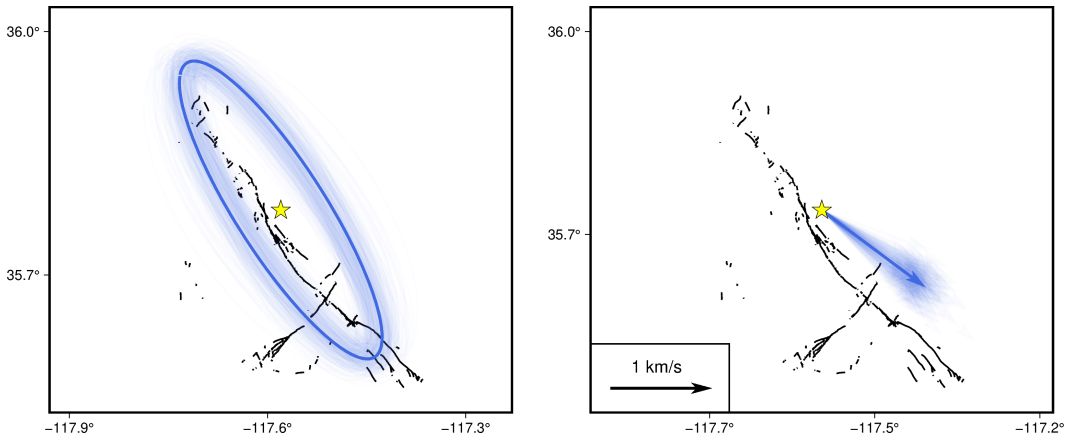

Figure 8. Summary figure of the map-view spatial and directivity features of the 2019 Ridgecrest mainshock as derived from the second moment inversion. Left: Map-view projections of a 500-solution subset of the ensemble of second spatial moment ellipsoids solved for in this study. Ellipsoids are defined using $r_c(\hat{\mathbf{n}})$ in equation 3. Right: Map-view projections of a 500-solution subset of the ensemble of $\mathbf{v_0}$, as defined in equation 4, solved for in this study. Black lines represent the surface-rupture faults mapped after the Ridgecrest mainshock. Yellow star marks the location of the gCMT centroid of the Ridgecrest mainshock. Transparent blue lines represent a single solution from the ensemble of second moment solutions. Solid blue lines represent the mean solution from the ensemble second moment solutions.

5 Discussion

When evaluating the solutions described in Figures 4, 7, and 8 and when contextualizing these solutions with previous results, it is important to keep in mind that these quantities are derived parameters from the variance of the stress glut distribution. This is distinct from other types of source parameterizations, such as finite-fault slip distributions, which attempt to solve for an approximation of the full stress glut distribution. Thus, the solutions presented in this study, while physically meaningful, ought to be considered as a separate category of rupture parameterization that should be compared to other rupture parameterizations cautiously. With this in mind, we can begin to assess whether the solutions given in this study yield a reasonable low-dimensional story of the Ridgecrest mainshock rupture.

In general, the ensemble of solutions for the Ridgecrest mainshock is well constrained and largely agrees with what is already known about the event. As is shown in Figure 8, the largest principal axis of the ellipsoid representation is well-aligned with the faults that are known to have ruptured during the mainshock. Additionally, the characteristic length of this rupture is in close agreement with the bulk of estimates of rupture extent for this earthquake. Also shown in Figure 8, the directivity vectors are aligned with these faults and suggest a rupture scenario in which the instantaneous centroid propagates from the NW to the SE. This unilateral behavior is in agreement with other estimates of the directivity of the event. The characteristic durations for this event, which suggest the period of time in which the majority of the moment, but importantly not all of the moment, was released, is also in agreement with other estimates of duration for this earthquake.

The joint probability distributions shown in Figures 2 and 5 suggest that most of the independent parameters of the second moments of the stress glut are weakly correlated. In general, this weak correlation suggests that a perturbation in one parameter will likely have little effect on the values of other parameters. Perhaps most interesting are the weak correlations between the spatial second moments and the mixed second moments and the

weak correlations between the spatial second moments and the temporal second moments. These suggest the intuitive conclusion that changing the velocity of the centroid, which is related to the velocity of rupture, changes the volume that can be ruptured in a given amount of time, and changing the amount of time available for rupture changes the volume through which a rupture of fixed velocity can propagate.

The low dimensional second moment estimate of the 2019 Ridgecrest mainshock illustrates the unique potential of this methodology for producing probabilistic estimates of finite source properties with few a priori assumptions on the fault geometry and rupture dynamics. The only requirement is a centroid moment tensor solution, which fits nicely into this framework, as the zeroth and first moments represent the scalar moment and centroid position of the earthquake respectively. In fact, the centroid moment tensor solution may be solved concurrently with the second moment solution (McGuire et al., 2000), but this introduces nonlinearity and significant additional computational/numerical complexity, which we reserve for future studies. The only constraint required in the inversion is that the source be non-negative in extent, which does not exclude any possible source scenarios. However, it is indeed easy to impose additional constraints on the second moments through the use of informed priors on the inversion parameters. Such informed priors should be imposed with the understanding that the second moments describe a covariance matrix of a 4-dimensional stress glut distribution. That is, informed priors are not necessarily being placed on the possible source dimensions, but instead are being placed on the possible covariances of the source distribution.

The 2019 Ridgecrest mainshock is a well-studied event, and many of the features of the rupture that are illuminated by this inversion were already known. However, this study serves as an illustration of some key strengths of this technique. Firstly, this methodology provides an estimate of the full posterior distribution of these solutions. So, claims regarding rupture finiteness can be made in the context of the full range of possible solutions given the uncertainty in the problem. Having a posterior distribution thus allows us to apply some degree of confidence to specific claims about an earthquake rupture. Consequently, with this methodology, we can make probabilistically supported assessments of the significance of similarities and differences between solutions for different events. Another benefit of this approach is that, given a prescribed correlation structure in the data, the data covariance matrix is solved for as a hyperparameter in the inversion. This means that the uncertainty of the posterior is reflective of data uncertainty that is solved for dynamically according to the structure of the data and the model.

Additionally, this methodology requires few of the a priori assumptions that present challenges and inaccuracies in other source finiteness estimation techniques, like finite-fault slip distributions. For example, this inversion technique does not require any prior characterization of the fault surface. Although the fault surface for Ridgecrest is well-approximated, for many global events, like offshore earthquakes, determining a fault surface is challenging, and so this methodology presents a substantial advantage for these events. Indeed, this methodology does not even require that all of the slip take place on a surface, but instead allows for moment release in a volume. This is apparent in Figure 8, where the spatial second moment is represented as an ellipsoid with significant width orthogonal to the major axis of the ellipsoid. Indeed, with this methodology, scientifically interesting properties like the fault-normal width of rupture can be probabilistically constrained and compared between events.

Another strength of this methodology is implicit in the fact that we employed this methodology using only GSN teleseismic data. Although the Ridgecrest earthquake occurred in an exceptionally well-instrumented area, for many global events teleseismic data is the only available information for characterizing the coseismic rupture. Thus for numerous events, given this limitation in data availability, robust information concerning rupture finiteness is scarce. This methodology then serves as a potentially pivotal tool in discerning probabilistic characterizations of earthquakes globally. Relatedly, large global events occur

infrequently, and thus historic events are a crucial component in our understanding of large earthquakes. The continuity of teleseismic data collection by the GSN for over two decades thus allows for this methodology to be readily applied to a large number of previous global earthquakes.

6 Conclusions

In this study, we develop a Bayesian framework for computing second moments of the stress glut of earthquakes using teleseismic data. This framework incorporates a positive-definite constraint under Cholesky decomposition and employs Hamiltonian Monte Carlo sampling to efficiently probe the parameter space. This methodology provides robust estimates of uncertainty by sampling the posterior distribution of solutions with dynamic error computation and accounting for the temporal correlation structure in the waveform data. These second moments of the stress glut provide a low-dimensional, physically-motivated representation of source volume, directivity, and duration that requires no *a priori* assumptions and is repeatable and comparable between events. We verify this methodology using a synthetic test and apply this framework to the 2019 Ridgecrest Sequence mainshock. We show that our solutions for this event yield event parameters that largely agree with what is known about this event and includes an estimate of the full posterior distribution. Our solution also illustrates some key strengths of this rupture-parameterization, namely the independence of this solution from a prescribed fault surface and the reliance of this inversion on only teleseismic data.

Acknowledgments

This work was partially funded by the National Science Foundation's (NSF) Graduate Research Fellowships Program (GRFP) under grant number DGE-1745301. The teleseismic waveforms used in this study are from the Global Seismographic Network (GSN) operated by Scripps Institution of Oceanography (II: IRIS/IDA; https://doi.org/10.7914/SN/II) (Scripps Institution Of Oceanography, 1986) and the Albuquerque Seismological Laboratory (IU: IRIS/USGS; https://doi.org/10.7914/SN/IU) (Albuquerque Seismological Laboratory (ASL)/USGS, 1988). These waveforms and associated metadata used in this study were accessed through the IRIS Data Management Center (DMC). The centroid and moment tensor solution used in this study were obtained from Global Centroid Moment Tensor (gCMT) catalog (Dziewonski et al., 1981; Ekström et al., 2012) at https://www.globalcmt.org/. The synthetic waveforms used in this study were generated using the software Salvus, (Afanasiev et al., 2019), available at https://mondaic.com/. Figure 1 was generated using The Generic Mapping Tools (GMT), version 6 (Wessel et al., 2019), available at https://www.generic-mapping-tools.org/. We would like to thank Dr. Hiroo Kanamori for sharing his experience and providing perceptive comments. We would also like to thank two anonymous reviewers for their inightful comments which greatly improved this manuscript, and the editor Dr. Rachel Abercrombie for facilitating the review process.

References

Afanasiev, M., Boehm, C., van Driel, M., Krischer, L., Rietmann, M., May, D. A., ... Fichtner, A. (2019). Modular and flexible spectral-element waveform modelling in two and three dimensions. *Geophysical Journal International*, *216*(3), 1675-1692. doi: 10.1093/gji/ggy469

Albuquerque Seismological Laboratory (ASL)/USGS. (1988). *Global Seismograph Network (GSN - IRIS/USGS)*. International Federation of Digital Seismograph Networks. Retrieved from `http://www.fdsn.org/doi/10.7914/SN/IU` doi: 10.7914/SN/IU

Ammon, C. J. (2005, May). Rupture process of the 2004 Sumatra-Andaman Earthquake. *Science*, *308*(5725), 1133–1139. Retrieved 2021-06-21, from `https://www.sciencemag.org/lookup/doi/10.1126/science.1112260` doi: 10.1126/science.1112260

Backus, G., & Mulcahy, M. (1976a, August). Moment tensors and other phenomenological descriptions of seismic sources–I. Continuous displacements. *Geophysical Journal International*, *46*(2), 341–361. Retrieved 2020-11-05, from `https://academic.oup.com/gji/article-lookup/doi/10.1111/j.1365-246X.1976.tb04162.x` doi: 10.1111/j.1365-246X.1976.tb04162.x

Backus, G., & Mulcahy, M. (1976b, November). Moment tensors and other phenomenological descriptions of seismic sources–II. Discontinuous displacements. *Geophysical Journal International*, *47*(2), 301–329. Retrieved 2020-11-05, from `https://academic.oup.com/gji/article-lookup/doi/10.1111/j.1365-246X.1976.tb01275.x` doi: 10.1111/j.1365-246X.1976.tb01275.x

Backus, G. E. (1977, October). Interpreting the seismic glut moments of total degree two or less. *Geophysical Journal International*, *51*(1), 1–25. Retrieved 2020-11-05, from `https://academic.oup.com/gji/article-lookup/doi/10.1111/j.1365-246X.1977.tb04187.x` doi: 10.1111/j.1365-246X.1977.tb04187.x

Barnhart, W. D., Hayes, G. P., & Gold, R. D. (2019, November). The July 2019 Ridgecrest, California, Earthquake Sequence: Kinematics of Slip and Stressing in Cross-Fault Ruptures. *Geophysical Research Letters*, *46*(21), 11859–11867. Retrieved 2021-11-09, from `https://onlinelibrary.wiley.com/doi/10.1029/2019GL084741` doi: 10.1029/2019GL084741

Bukchin, B. (1995, August). Determination of stress glut moments of total degree 2 from teleseismic surface wave amplitude spectra. *Tectonophysics*, *248*(3-4), 185–191. Retrieved 2020-11-05, from `https://linkinghub.elsevier.com/retrieve/pii/004019519400271A` doi: 10.1016/0040-1951(94)00271-A

Chen, P. (2005, June). Finite-moment tensor of the 3 September 2002 Yorba Linda Earth-

quake. *Bulletin of the Seismological Society of America*, *95*(3), 1170–1180. Retrieved 2020-11-05, from https://pubs.geoscienceworld.org/bssa/article/95/3/1170-1180/103154 doi: 10.1785/0120040094

Dahlen, F., & Tromp, J. (1998). *Theoretical global seismology.* Princeton, N.J.: Princeton University Press.

Du, Y., Aydin, A., & Segall, P. (1992, August). Comparison of various inversion techniques as applied to the determination of a geophysical deformation model for the 1983 Borah Peak Earthquake. *Bulletin of the Seismological Society of America*, *82*(4), 1840–1866.

Duputel, Z., Agram, P. S., Simons, M., Minson, S. E., & Beck, J. L. (2014, April). Accounting for prediction uncertainty when inferring subsurface fault slip. *Geophysical Journal International*, *197*(1), 464–482. Retrieved 2020-11-03, from http://academic.oup.com/gji/article/197/1/464/686313/Accounting-for-prediction-uncertainty-when doi: 10.1093/gji/ggt517

DuRoss, C. B., Gold, R. D., Dawson, T. E., Scharer, K. M., Kendrick, K. J., Akciz, S. O., ... Zinke, R. (2020, August). Surface Displacement Distributions for the July 2019 Ridgecrest, California, Earthquake Ruptures. *Bulletin of the Seismological Society of America*, *110*(4), 1400–1418. Retrieved 2021-11-09, from https://pubs.geoscienceworld.org/ssa/bssa/article/110/4/1400/587507/Surface-Displacement-Distributions-for-the-July doi: 10.1785/0120200058

Dziewonski, A. M., Chou, T. A., & Woodhouse, J. H. (1981, April). Determination of earthquake source parameters from waveform data for studies of global and regional seismicity. *Journal of Geophysical Research: Solid Earth*, *86*(B4), 2825–2852. Retrieved 2020-11-05, from http://doi.wiley.com/10.1029/JB086iB04p02825 doi: 10.1029/JB086iB04p02825

Ekström, G., Nettles, M., & Dziewoński, A. (2012, June). The global CMT project 2004–2010: Centroid-moment tensors for 13,017 earthquakes. *Physics of the Earth and Planetary Interiors*, *200-201*, 1–9. Retrieved 2020-11-05, from https://linkinghub.elsevier.com/retrieve/pii/S0031920112000696 doi: 10.1016/j.pepi.2012.04.002

GCMT. (2019). *Mw 7.0 central california.* Retrieved from https://www.globalcmt.org/cgi-bin/globalcmt-cgi-bin/CMT5/form?itype=ymd&yr=2019&mo=07&day=1&otype=ymd&oyr=2019&omo=07&oday=10&jyr=1976&jday=1&ojyr=1976&ojday=1&nday=1&lmw=7&umw=10&lms=0&ums=10&lmb=0&umb=10&llat=-90&ulat=90&llon=-180&ulon=180&lhd=0&uhd=1000&lts=-9999&uts=9999&lpe1=0&upe1=90&lpe2=0&upe2=90&list=0

Gelman, A., Carlin, J., Stern, H., Dunson, D., Vehtari, A., & Rubin, D. (2010). *Bayesian data analysis.* Boca Raton, F.L.: Chapman and Hall-CRC Press.

Gelman, A., & Rubin, D. (1992). Inference from iterative simulation using multiple sequences. *Statistical Science*, *7*(4), 457–511.

Goldberg, D. E., Melgar, D., Sahakian, V. J., Thomas, A. M., Xu, X., Crowell, B. W., & Geng, J. (2020, February). Complex Rupture of an Immature Fault Zone: A Simultaneous Kinematic Model of the 2019 Ridgecrest, CA Earthquakes. *Geophysical Research Letters*, *47*(3). Retrieved 2021-11-09, from https://onlinelibrary.wiley.com/doi/10.1029/2019GL086382 doi: 10.1029/2019GL086382

Hartzell, S. H., & Heaton, T. H. (1983, December). Inversion of strong ground motion and teleseismic waveform data for the fault rupture history of the 1979 Imperial Valley, California Earthquake. *Bulletin of the Seismological Society of America*, *73*(6), 1553–1583.

Ide, S., Baltay, A., & Beroza, G. C. (2011, June). Shallow Dynamic Overshoot and Energetic Deep Rupture in the 2011 Mw 9.0 Tohoku-Oki Earthquake. *Science*, *332*(6036), 1426–1429. Retrieved 2021-06-21, from https://www.sciencemag.org/lookup/doi/10.1126/science.1207020 doi: 10.1126/science.1207020

Innes, M. (2019, March). Don't Unroll Adjoint: Differentiating SSA-Form Programs. *arXiv:1810.07951 [cs]*. Retrieved 2021-06-29, from http://arxiv.org/abs/1810

.07951 (arXiv: 1810.07951)

Jia, Z., Wang, X., & Zhan, Z. (2020, September). Multifault Models of the 2019 Ridgecrest Sequence Highlight Complementary Slip and Fault Junction Instability. *Geophysical Research Letters*, *47*(17). Retrieved 2021-11-09, from https://onlinelibrary.wiley.com/doi/10.1029/2020GL089802 doi: 10.1029/2020GL089802

Jin, Z., & Fialko, Y. (2020, August). Finite Slip Models of the 2019 Ridgecrest Earthquake Sequence Constrained by Space Geodetic Data and Aftershock Locations. *Bulletin of the Seismological Society of America*, *110*(4), 1660–1679. Retrieved 2021-11-09, from https://pubs.geoscienceworld.org/ssa/bssa/article/110/4/1660/587725/Finite-Slip-Models-of-the-2019-Ridgecrest doi: 10.1785/0120200060

Lay, T. (2018, May). A review of the rupture characteristics of the 2011 Tohoku-oki Mw 9.1 earthquake. *Tectonophysics*, *733*, 4–36. Retrieved 2021-06-21, from https://linkinghub.elsevier.com/retrieve/pii/S0040195117303992 doi: 10.1016/j.tecto.2017.09.022

Lee, E.-J., Chen, P., Jordan, T. H., & Wang, L. (2011, July). Rapid full-wave centroid moment tensor (CMT) inversion in a three-dimensional earth structure model for earthquakes in Southern California: Rapid full-wave CMT inversion. *Geophysical Journal International*, *186*(1), 311–330. Retrieved 2021-06-21, from https://academic.oup.com/gji/article-lookup/doi/10.1111/j.1365-246X.2011.05031.x doi: 10.1111/j.1365-246X.2011.05031.x

Liu, C., Lay, T., Brodsky, E. E., Dascher-Cousineau, K., & Xiong, X. (2019, November). Coseismic Rupture Process of the Large 2019 Ridgecrest Earthquakes From Joint Inversion of Geodetic and Seismological Observations. *Geophysical Research Letters*, *46*(21), 11820–11829. Retrieved 2021-11-09, from https://onlinelibrary.wiley.com/doi/10.1029/2019GL084949 doi: 10.1029/2019GL084949

McGuire, J. J. (2002, December). Predominance of Unilateral Rupture for a Global Catalog of Large Earthquakes. *Bulletin of the Seismological Society of America*, *92*(8), 3309–3317. Retrieved 2020-11-05, from https://pubs.geoscienceworld.org/bssa/article/92/8/3309-3317/103071 doi: 10.1785/0120010293

McGuire, J. J. (2004, April). Estimating Finite Source Properties of Small Earthquake Ruptures. *Bulletin of the Seismological Society of America*, *94*(2), 377–393. Retrieved 2020-11-05, from https://pubs.geoscienceworld.org/bssa/article/94/2/377-393/146918 doi: 10.1785/0120030091

McGuire, J. J., Zhao, L., & Jordan, T. H. (2000, August). Rupture dimensions of the 1998 Antarctic Earthquake from low-frequency waves. *Geophysical Research Letters*, *27*(15), 2305–2308. Retrieved 2020-11-05, from http://doi.wiley.com/10.1029/1999GL011186 doi: 10.1029/1999GL011186

McGuire, J. J., Zhao, L., & Jordan, T. H. (2001, June). Teleseismic inversion for the second-degree moments of earthquake space-time distributions. *Geophysical Journal International*, *145*(3), 661–678. Retrieved 2020-11-05, from https://academic.oup.com/gji/article-lookup/doi/10.1046/j.1365-246x.2001.01414.x doi: 10.1046/j.1365-246x.2001.01414.x

Meng, H., McGuire, J. J., & Ben-Zion, Y. (2020, April). Semiautomated estimates of directivity and related source properties of small to moderate Southern California earthquakes using second seismic moments. *Journal of Geophysical Research: Solid Earth*, *125*(4), e2019JB018566. Retrieved 2021-06-23, from https://onlinelibrary.wiley.com/doi/10.1029/2019JB018566 doi: 10.1029/2019JB018566

Minson, S. E., Simons, M., & Beck, J. L. (2013, September). Bayesian inversion for finite fault earthquake source models I—theory and algorithm. *Geophysical Journal International*, *194*(3), 1701–1726. Retrieved 2020-11-03, from http://academic.oup.com/gji/article/194/3/1701/645931/Bayesian-inversion-for-finite-fault-earthquake doi: 10.1093/gji/ggt180

Monelli, D., Mai, P. M., Jónsson, S., & Giardini, D. (2009, January). Bayesian imaging of the 2000 Western Tottori (Japan) earthquake through fitting of strong motion and GPS data. *Geophysical Journal International*, *176*(1), 135–150. Retrieved

2021-06-21, from https://academic.oup.com/gji/article-lookup/doi/10.1111/j.1365-246X.2008.03943.x doi: 10.1111/j.1365-246X.2008.03943.x

Moreno, M., Rosenau, M., & Oncken, O. (2010, September). 2010 Maule earthquake slip correlates with pre-seismic locking of Andean subduction zone. *Nature*, *467*(7312), 198–202. Retrieved 2021-06-21, from http://www.nature.com/articles/nature09349 doi: 10.1038/nature09349

Moulik, P., & Ekström, G. (2014, December). An anisotropic shear velocity model of the Earth's mantle using normal modes, body waves, surface waves and long-period waveforms. *Geophysical Journal International*, *199*(3), 1713–1738. Retrieved 2021-11-04, from http://academic.oup.com/gji/article/199/3/1713/617840/An-anisotropic-shear-velocity-model-of-the-Earths doi: 10.1093/gji/ggu356

Neal, R. (2010). *MCMC using Hamiltonian Dynamics.* Boca Raton, F.L.: Chapman and Hall-CRC Press.

Ponti, D. J., Blair, J. L., Rosa, C. M., Thomas, K., Pickering, A. J., Akciz, S., ... Zinke, R. (2020, September). Documentation of Surface Fault Rupture and Ground-Deformation Features Produced by the 4 and 5 July 2019 Mw 6.4 and Mw 7.1 Ridgecrest Earthquake Sequence. *Seismological Research Letters*, *91*(5), 2942–2959. Retrieved 2021-11-09, from https://pubs.geoscienceworld.org/ssa/srl/article/91/5/2942/588337/Documentation-of-Surface-Fault-Rupture-and doi: 10.1785/0220190322

Ross, Z. E., Idini, B., Jia, Z., Stephenson, O. L., Zhong, M., Wang, X., ... Jung, J. (2019, October). Hierarchical interlocked orthogonal faulting in the 2019 Ridgecrest earthquake sequence. *Science*, *366*(6463), 346–351. Retrieved 2021-11-09, from https://www.science.org/doi/10.1126/science.aaz0109 doi: 10.1126/science.aaz0109

Saito, T., Ito, Y., Inazu, D., & Hino, R. (2011, April). Tsunami source of the 2011 Tohoku-Oki earthquake, Japan: Inversion analysis based on dispersive tsunami simulations. *Geophysical Research Letters*, *38*(7), L00G19. Retrieved 2021-06-21, from http://doi.wiley.com/10.1029/2011GL049089 doi: 10.1029/2011GL049089

Scripps Institution Of Oceanography. (1986). *IRIS/IDA Seismic Network.* International Federation of Digital Seismograph Networks. Retrieved from http://www.fdsn.org/doi/10.7914/SN/II doi: 10.7914/SN/II

Silver, P. G., & Jordan, T. H. (1983). Total-moment spectra of fourteen large earthquakes. *Journal of Geophysical Research*, *88*(B4), 3273. Retrieved 2020-11-05, from http://doi.wiley.com/10.1029/JB088iB04p03273 doi: 10.1029/JB088iB04p03273

Tarantola, A. (2005). *Inverse Problem Theory and Methods for Model Parameter Estimation.* Society for Industrial and Applied Mathematics. Retrieved 2020-11-03, from http://epubs.siam.org/doi/book/10.1137/1.9780898717921 doi: 10.1137/1.9780898717921

USGS. (2019). *M 7.1 - 2019 ridgecrest earthquake sequence.* Retrieved from https://earthquake.usgs.gov/earthquakes/eventpage/ci38457511/moment-tensor?source=us&code=us_70004bn0_mww

USGS, & CGS. (2021). *Quaternary fault and fold database for the united states.* Retrieved from https://www.usgs.gov/natural-hazards/earthquake-hazards/faults

Vallée, M., & Douet, V. (2016, August). A new database of source time functions (STFs) extracted from the SCARDEC method. *Physics of the Earth and Planetary Interiors*, *257*, 149–157. Retrieved 2020-11-03, from https://linkinghub.elsevier.com/retrieve/pii/S0031920116300735 doi: 10.1016/j.pepi.2016.05.012

Wald, D. J., & Heaton, T. H. (1992). Spatial and temporal distribution of slip for the 1992 Landers, California, Earthquake. *Bulletin of the Seismological Society of America*, *84*(3), 668–691.

Walsh, D., Arnold, R., & Townend, J. (2009, January). A Bayesian approach to determining and parametrizing earthquake focal mechanisms. *Geophysical Journal International*, *176*(1), 235–255. Retrieved 2021-06-21, from https://academic.oup.com/gji/article-lookup/doi/10.1111/j.1365-246X.2008.03979.x doi: 10.1111/j.1365-246X.2008.03979.x

Wang, K., Dreger, D. S., Tinti, E., Bürgmann, R., & Taira, T. (2020, Au-

gust). Rupture Process of the 2019 Ridgecrest, California Mw 6.4 Foreshock and Mw 7.1 Earthquake Constrained by Seismic and Geodetic Data. *Bulletin of the Seismological Society of America*, *110*(4), 1603–1626. Retrieved 2021-11-09, from https://pubs.geoscienceworld.org/ssa/bssa/article/110/4/1603/587915/Rupture-Process-of-the-2019-Ridgecrest-California doi: 10.1785/0120200108

Wessel, P., Luis, J. F., Uieda, L., Scharroo, R., Wobbe, F., Smith, W. H. F., & Tian, D. (2019). *The generic mapping tools.* Retrieved from https://www.generic-mapping-tools.org/

Wéber, Z. (2006, May). Probabilistic local waveform inversion for moment tensor and hypocentral location. *Geophysical Journal International*, *165*(2), 607–621. Retrieved 2021-06-21, from https://academic.oup.com/gji/article-lookup/doi/10.1111/j.1365-246X.2006.02934.x doi: 10.1111/j.1365-246X.2006.02934.x

Xie, Y., Bao, H., & Meng, L. (2021, October). Source Imaging With a Multi-Array Local Back-Projection and Its Application to the 2019 M_w 6.4 and M_w 7.1 Ridgecrest Earthquakes. *Journal of Geophysical Research: Solid Earth*, *126*(10). Retrieved 2021-11-09, from https://onlinelibrary.wiley.com/doi/10.1029/2020JB021396 doi: 10.1029/2020JB021396

Xu, X., Sandwell, D. T., & Smith-Konter, B. (2020, July). Coseismic Displacements and Surface Fractures from Sentinel-1 InSAR: 2019 Ridgecrest Earthquakes. *Seismological Research Letters*, *91*(4), 1979–1985. Retrieved 2021-11-09, from https://pubs.geoscienceworld.org/ssa/srl/article/91/4/1979/580045/Coseismic-Displacements-and-Surface-Fractures-from doi: 10.1785/0220190275

Yue, H., Sun, J., Wang, M., Shen, Z., Li, M., Xue, L., ... Lay, T. (2021, September). The 2019 Ridgecrest, California earthquake sequence: Evolution of seismic and aseismic slip on an orthogonal fault system. *Earth and Planetary Science Letters*, *570*, 117066. Retrieved 2021-11-09, from https://linkinghub.elsevier.com/retrieve/pii/S0012821X21003216 doi: 10.1016/j.epsl.2021.117066